Metal–Organic Frameworks |Hot Paper|

Chromium Speciation in Zirconium-Based Metal–Organic Frameworks for Environmental Remediation

Paula G. Saiz[+,[a, i]] Naroa Iglesias[+,[a]] Bárbara González Navarrete,[b] Maibelin Rosales,[b] Yurieth Marcela Quintero,[b] Ander Reizabal,[a] Joseba Orive,[c] Arkaitz Fidalgo Marijuan,[a, d] Edurne S. Larrea,[e, f] Ana Catarina Lopes,[a] Luis Lezama,[g] Andreina García,*[b] Senentxu Lanceros-Mendez,[a, h] María Isabel Arriortua,[a, i] and Roberto Fernández de Luis[+*[a]]

Abstract: Acute Cr^{VI} water pollution due to anthropogenic activities is an increasing worldwide concern. The high toxicity and mobility of Cr^{VI} makes it necessary to develop dual adsorbent/ion-reductive materials that are able to capture Cr^{VI} and transform it efficiently into the less hazardous Cr^{III}. An accurate description of chromium speciation at the adsorbent/ion-reductive matrix is key to assessing whether Cr^{VI} is completely reduced to Cr^{III}, or if its incomplete transformation has led to the stabilization of highly reactive, transient Cr^{V} species within the material. With this goal in mind, a dual ultraviolet–visible and electron paramagnetic spectroscopy approach has been applied to determine the chromium speciation within zirconium-based metal–organic frameworks (MOFs). Our findings point out that the generation of defects at Zr-MOFs boosts Cr^{VI} adsorption, whilst the presence of reductive groups on the organic linkers play a key role in stabilizing it as isolated and/or clustered Cr^{III} ions.

Introduction

Water pollution by heavy metals derived from natural leaching of geologic bedrocks and mining activities is one of the biggest environmental issues to be faced in the 21st century.[1–3] Apart from their high toxicity, even at very low concentrations, heavy metals are non-biodegradable, highly mobile and present a long-term bio-persistence, which makes them an increasing environmental and health concern.[3–5]

Within the heavy metals, chromium is particularly dangerous as it is usually present as highly soluble and mobile hexavalent chromate ($[Cr^{VI}O_4]^{2-}$) and dichromate ($(Cr_2^{VI}O_7)^{2-}$) oxyanions, which are genotoxic, mutagenic, teratogenic and carcinogenic.[2] The scientific community is paying attention to this environmental problem, focusing efforts on the development of bifunctional materials that are able to work as Cr^{VI} sorbents and Cr^{VI} to Cr^{III} reducers.[6–12]

An accurate description of chromium speciation at the sorbent/reductive matrix is key to estimating the chromium reduction efficiency of these bifunctional porous materials.[13–15] More specifically, an accurate chromium speciation description is required to quantitatively assess whether the Cr^{VI} species has been completely reduced to Cr^{III}, or if a mixture of hexavalent chromium and/or intermediate reactive Cr^{V} species has been

[a] P. G. Saiz,[+] N. Iglesias,[+] A. Reizabal, Dr. A. Fidalgo Marijuan, Dr. A. C. Lopes, Prof. S. Lanceros-Mendez, Prof. M. I. Arriortua, Dr. R. Fernández de Luis[+]
BCMaterials, Basque Center for Materials, Applications and Nanostructures
UPV/EHU Science Park, 48940 Leioa (Spain)
E-mail: roberto.fernandez@bcmaterials.net

[b] B. González Navarrete, M. Rosales, Y. M. Quintero, Dr. A. García
Department Water, Environment and Sustainability
Advanced Mining Technology Center (AMTC)
Facultad de Ciencias FísicasyMatemáticas, Universidad de Chile
Av. Tupper 2007, Santiago (Chile)
E-mail: andreina.garcia@amtc.cl

[c] Dr. J. Orive
Dept. of Chemical Engineering, Biotechnology and Materials
Facultad de Ciencias Físicas y Matemáticas, Universidad de Chile
Av. Beauchef 851, Santiago (Chile)

[d] Dr. A. Fidalgo Marijuan
Dept. of Organic Chemistry II, Science and Technology Faculty
University of the Basque Country (UPV/EHU)
Barrio Sarriena s/n, Leioa, Bizkaia 48940 (Spain)

[e] Dr. E. S. Larrea
Le Studium Research Fellow
Loire Valley Institute for Advanced Studies, Orléans and Tours (France)

[f] Dr. E. S. Larrea
CEMHTI—UPR3079 CNRS
1 avenue de la Recherche Scientifique, 45100 Orléans (France)

[g] Prof. L. Lezama
Department of Inorganic Chemistry, Science and Technology Faculty
University of the Basque Country (UPV/EHU)
Barrio Sarriena s/n, Leioa, Bizkaia 48940 (Spain)

[h] Prof. S. Lanceros-Mendez
IKERBASQUE Basque Foundation for Science, 48013 Bilbao (Spain)

[i] P. G. Saiz,[+] Prof. M. I. Arriortua
Department of Mineralogy and Petrology, Science and Technology Faculty
University of the Basque Country (UPV/EHU)
Barrio Sarriena s/n, Leioa, Bizkaia 48940 (Spain)

[+] These authors contributed equally to this work.

Supporting information and the ORCID identification number(s) for the author(s) of this article can be found under: https://doi.org/10.1002/chem.202001435.

stabilized within the sorbent.[16] This is particularly relevant for Cr^{V}, as even if it is immobilized at the sorbent/reductive-matrix, pentavalent chromium is able to generate oxidizing species that damage RNA and/or DNA.[17–20]

The quantification of the chromium adsorbed within a porous material has been usually determined by energy-dispersive X-ray spectroscopy (EDX) or inductively coupled plasma atomic emission spectroscopy (ICP).[21,22] Nevertheless, these techniques fail to determine the chromium oxidation state once it is immobilized at the sorbent. More detailed information of the chromium oxidation and speciation can be obtained by X-ray photoelectron spectroscopy (XPS),[13] but XPS is still a surface technique that fails detecting low concentrated and/or transient chromium species.[23,24] In order to obtain a deeper insight, it is necessary to perform X-ray adsorption experiments (XAS) to experimentally determine an accurate description of the chromium local structure and oxidation state.[25–28] Nevertheless, it is worth noticing that XAS experimental technique is only available at large installation facilities, and that it fails to differentiate between different chromium species when a complex Cr^{VI}, Cr^{V} and Cr^{III} mixture is found. Therefore, a precise chromium speciation description would require from the combination of specific techniques that allow i) distinguishing between the oxidation states of chromium ions and ii) obtaining information about the local structure of low concentrated chromium species.

In this work, a combination of ultraviolet–visible (UV/Vis) and electron paramagnetic resonance spectroscopy (EPR) techniques is proposed to describe the chromium speciation after a coupled adsorption and reduction process in metal–organic frameworks (MOFs).[23,29–31] UV/Vis spectral fingerprints of Cr^{VI} and Cr^{III} species are easily distinguishable, a feature that gives qualitative information of chromium coordination environment.[30,32,33] Complementarily, EPR spectroscopy is highly sensitive to the detection of transient Cr^{V}, as well as it is highly effective in detecting the presence of Cr^{III} as isolated or clustered species.[34] Thus, in combination, UV/Vis and EPR provide a complete snapshot of the Cr^{VI}-Cr^{V}-Cr^{III} speciation at the MOF structures.

Zirconium based MOFs, and in particular the archetypal zirconium terephthalate family (i.e., *UiO-66*), has been selected as the matrix to develop this study. UiO-66 is built up from $Zr_6O_4(OH)_4(\text{-}COOH)_{12}$ hexanuclear clusters connected through twelve terephthalate type organic linkers.[27,35–40] In addition to their chemical stability and microporous structure, both inorganic and organic structural units are easily tuneable with chemical motifs or properties that can trigger the chromium reduction. In addition, depending on the synthesis conditions, linker defects can be generated within the structure, which can reduce the clusters connectivity from twelve to eight linkers too (Scheme 1 A).[28,41–43] This random linker removal is defined as "defect engineering", and it is well-known to significantly affect the porosity and the adsorption/reduction dual capacity of Zr-MOFs. Indeed, oxyanion adsorption capacity of UiO-66 type materials is highly dependent on their defect density degree, as the under-coordinated positions are preferential chemisorption points of oxyanions (Scheme 1 A, B).[44–48]

Generally speaking, two approaches have been applied in Zr based MOFs in order to endow them of a dual adsorption/ion-reductive functionality: i) the organic pillars decoration with electron-donor groups that trigger the chromium reduction[49–51] (Scheme 1 C) and ii) the use of photoactive building blocks that are able to generate radicals to trigger the Cr^{VI} to Cr^{III} transformation.[21,52–56] Therefore, depending on the chemical information encoded within the UiO-66 framework, its Cr^{VI} adsorption and, more specifically, its ion-reductive capacity can be regulated to different extents. This modulation of a specific chemical property enables the after-operation study of diverse Cr speciation scenarios (Scheme 1 B, C). Indeed, our findings point that depending on the chemical encoding, chromium can be found within UiO-66 materials as hexavalent species just immobilized at the structure, as intermediate semi-reduced complex Cr^{VI}, Cr^{V} and Cr^{III} mixtures, or as completely reduced Cr^{III} isolated or clustered ions (Scheme 1 C).

In this work, we have investigated the Cr^{VI} dual adsorption/ion-reductive efficiency of six different Zr-terephthalate crystal frameworks named as UiO-66, UiO-66-def, UiO-66-$(OH)_2$, UiO-66-$(OH)_2$-def, UiO-66-NH_2 and UiO-66-NH_2-def (defective structures have been labelled with a "-def" suffix in their code). The bifunctionality of the UiO-66 materials has been achieved through: i) the linker defects generation, which are known to be efficient adsorption positions for Cr^{VI}; ii) the electron-donor groups incorporation (i.e., -$(OH)_2$, -NH_2) at the organic linkers, which work as active functionalities that can directly trigger the Cr^{VI} to Cr^{III} reduction, and finally, iii) the combination of the adsorption and posterior photo-reduction of Cr^{VI} to Cr^{III} for the

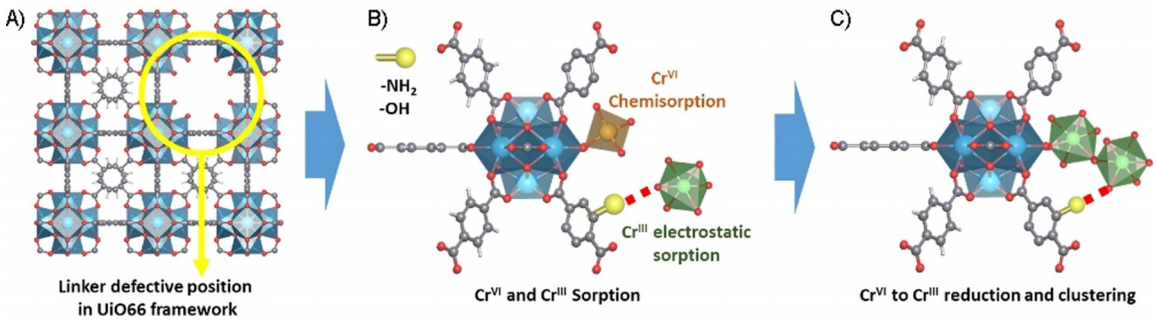

Scheme 1. A) Possible local structure of a linker defect position in a UiO-66 zirconium terephthalate framework. B) Detail of the possible Cr^{VI} and Cr^{III} adsorption positions at an under-coordinated defect position and organic linkers of zirconium hexanuclear local structure. C) Cr^{VI} to Cr^{III} reduction induced by the presence of electron-donor groups at the organic linkers or photoactivity of the material. Hydrogen atoms have been omitted for clarity.

specific case of photoactive UiO-66-NH_2 material.[57–59] After operation, chromium speciation has been fully determined by means of UV/Vis and EPR spectroscopy, quantifying the Cr^{VI} to Cr^{III} reduction efficiency for each material. For comparison purpose, adsorption and posterior speciation analysis have been also studied for trivalent chromium species, in order to understand the possible chromium immobilization mechanisms in a hypothetical case of full Cr^{VI} to Cr^{III} transformation.

Results and Discussion

Synthesis and characterization

A set of six UiO-66 derivatives has been solvothermally synthesized modifying the organic linker functionalization (UiO-66-R (R = -H, -NH_2, -$(OH)_2$), and linker defect density (UiO-66-R (R = -H-def, -NH_2-def,.$(OH)_2$-def)) of the crystal structures. Hydroxylated (UiO-66-$(OH)_2$) and amine (UiO-66-NH_2) analogue materials have been obtained applying the same synthesis conditions of UiO-66, but replacing the terephthalic acid reagent per equal molar amounts of 2,5-dihydroxyterephthalic acid (doBDC; 98%) and 2-aminoterephthalic acid (BDC-NH_2), respectively. Hydrochloric acid has been used as acid modulator to obtain analogue defective compounds (i.e., UiO-66-def, UiO-66-$(OH)_2$-def and UiO-66-NH_2-def) (Table S1, Figures S2–S4 in the Supporting Information). Together, the set covers a range of materials exhibiting the same crystal structure "fcu" topology shown by the archetypal UiO-66, but adding to the different materials the specific functionalities ascribed to the electron-donor groups and linker defect positions, which are expected to induce different chromate binding and reductive capacities.[57,60] Detailed information on the synthesis and characterization of the materials is provided as Supporting Information.

The quality of the UiO66-R materials, as well as the density of linker defects within them, were determined by applying multiple complementary characterization technique approach: X-ray diffraction (XRD, Figures 1A and S1), temperature dependent X-ray diffraction (TDX, Figures S11 and S12), Infrared spectroscopy (IR, Figures 1B and S9), thermogravimetric analyses (TGA, Figures 1C and S3), transmission electron microscopy (TEM, Figure S10) and nitrogen sorption measurements at 77 K (Figures 1D and S2).

First, powder XRD patterns were measured for all UiO-66-R materials (R=-H, -NH_2, -$(OH)_2$, -H-def, -NH_2-def, $(OH)_2$-def). The XRD patterns are fully consistent with the simulated data obtained from the UiO-66 structural model (Figure 1A).[42] Profile pattern matching analyses confirm no meaningful displacements of the cell parameters due to the organic linkers func-

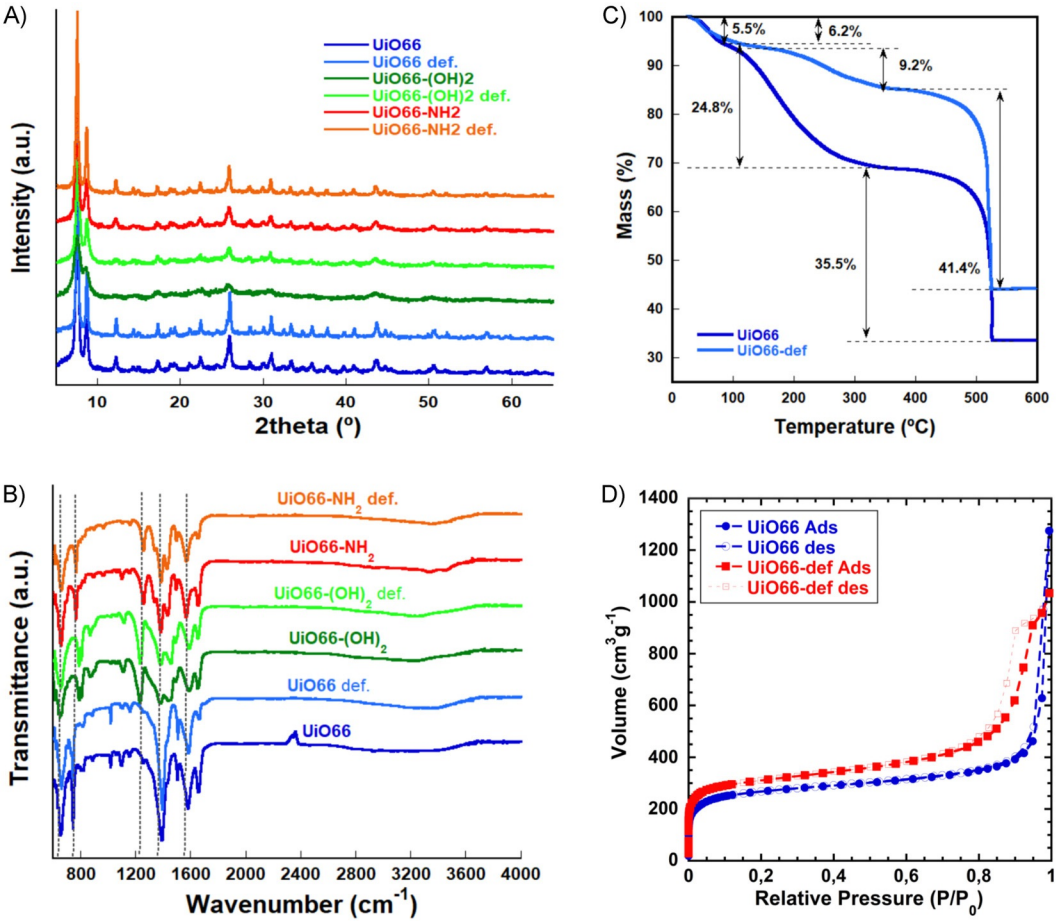

Figure 1. A) XRD patterns and B) FTIR-ATR spectra of the different samples before the chromium adsorption experiments. C) TGA curve for the UiO-66 and UiO-66-def samples and D) N_2 adsorption isotherms of the UiO-66 and UiO-66-def samples before the adsorption experiments.

tionalization and/or linker defects generation (Figure S1 and Table S2). Slight differences in the peak width, related to the particle size of the samples (confirmed by TEM analysis, Figure S10), were observed. In general terms, defective samples show more crystalline diffraction patterns, a fact that is related to the crystal-growth template effect of the HCl incorporation to the synthesis media.[46] In addition, slight broadening of the peak is observed for hydroxylated compounds in comparison to non-functionalized and amino bearing derivatives. FTIR spectra show the characteristic fingerprint bands of the UiO-66 structure (Figure 1 B), tentatively assigned to the longitudinal and transverse vibrational modes of the Zr–O bonds (at 745 and 660 cm^{-1}) or/and to the asymmetric and symmetric stretching vibrations of the carboxylate groups (1581 and 1389 cm^{-1}). In addition, phenolic adsorption bands related to the C–*O*–H stretching vibrations (1235 cm^{-1})[3] and (1258 and 1338 cm^{-1}) and to the vibrational modes of amino groups, have been identified for UiO-66-$(OH)_2$/UiO-66-$(OH)_2$-def and UiO-66-NH_2/UiO-66-NH_2-def samples, respectively. XRD and FTIR were also used to prove the stability of the six MOFs under the later used conditions to adsorb or photo-reduce chromate anions (Figures S6 and S7).

For additional bulk characterization, UiO66-R samples were examined with both N_2 sorption (77 K) experiments (Figure 1 D and S2) and TGA (Figures 1 C and S3). The results obtained from both techniques allow quantifying the defect degree within the structures, as well as determining its impact on the micro-porosity.

The TGA data exhibit three important weight loss steps. The first one, of about 5% (T = 30–100 °C), is related to the release of the solvent trapped within the porous framework. The second one has a weight loss value of about 10–20% (T = 100–280 °C) and it is related to the dehydroxylation and dehydration of the Zr-hexanuclear clusters. Therefore, at 280 °C, the UiO-66-R materials are foreseen to be stabilized in their completely dehydrated and de-hydroxylated forms, and hence fore, their formula at this temperature can be described as:

Zr_6O_{6+x}(linker)$_{6-x}$, where *"x"* stands for the linker defect positions in the structure. At 280 °C, the charge unbalance generated because of the linker defect presence is compensated by the incorporation of additional oxygen atoms in the Zr-hexanuclear cluster.[61,62]

Finally, the third step is ascribed to the calcination of the ligands, which finally induces the collapse of the crystal framework.[26,28] The linker-defect positions average per formula was estimated from the weight loss associated to this third step of the TGA curves (Figure S3). Assuming that: i) at 280 °C the zirconium hexanuclear clusters are completely dehydrated and dehydroxylated,[41] and ii) that the weight loss at higher temperatures is ascribed to the organic linker calcination. The theoretical weight loss for the linker calcination between 280 °C until 600 °C can be calculated based on Equation (1) (Figure S4 and Tables S3–S5):

$$Zr_6O_{6+x}(linker)_{6-x} \rightarrow Zr_6O_{12} \quad (1)$$

Different weight losses were calculated varying the linker defect degree of the UiO-66-R compounds, and afterwards, the obtained weight loss versus linker defect data were plotted in the Figure S4. The calculated data can be fitted to a linear equation that was used to determine the experimental defects per formula from the experimental weight loss observed at 280 °C, after normalizing it to 100% (Figure S3 d, e). The results are summarized in the Table 1. The calculated defect density per formula vary from 0.9–1.1 for "nondefective" samples and to 1.1–2.3 in defective ones. This trend confirms the defect template effect of the HCl addition during the synthesis. It is worth noting that the "non-defective" samples also present some degree of linker missing defects, as derived from TGA results.

Based on the determined defect degree, the chemical formulas for the completely dehydrated and dehydroxylated compounds have been also proposed in the Table 1. In addition, the chemical formulas of the compounds at room temperature have been also described in the Table 1. For that, it has been assumed that in order to maintain the charge neutrality, each carboxyl defective position in the cluster is compensated per a water molecule and hydroxy group pair.

The defect chemistry effect on the crystal framework of UiO-66 was also studied by means of N_2 adsorption-desorption isotherms at 77 K (Figure 1 D). The Brunauer–Emmett–Teller (BET) surface area was obtained from the fitting of the linearized form of BET equation (Figure S2). As expected, a slight increase on the surface area is induced due to the extra porosity generated at the linker vacancies within the crystal structures (UiO-66 = 1015 $m^2 g^{-1}$, UiO-66-def = 1165 $m^2 g^{-1}$).[37]

Table 1. Mass losses and proposed formula unit for each compound, as estimated from the thermogravimetric curves.

Sample	Tentative formula at room temperature	Dehydrated formula at 280 °C[b]	Experimental mass loss [%][a]	Calcd defects
UiO-66	$[Zr_6O_4(OH)_{5.8}(H_2O)_{1.8}(BDC)_{5.1}]$·solvent	$Zr_6O_{6.9}(BDC)_{5.1}$	52.40	0.9/6
UiO-66-$(OH)_2$	$[Zr_6O_4(OH)_{6.2}(H_2O)_{2.2}(doBDC)_{4.9}]$·solvent	$Zr_6O_{7.1}(doBDC)_{4.9}$	54.0	1.1/6
UiO-66-NH_2	$[Zr_6O_4(OH)_{4.6}(H_2O)_{0.6}(BDC\text{-}NH_2)_{5.7}]$·solvent	$Zr_6O_{6.3}(BDC\text{-}NH_2)_{5.7}$	53.2	0.3/6
UiO-66-def	$[Zr_6O_4(OH)_{7.0}(H_2O)_{3.0}(BDC)_{4.5}]$·solvent	$Zr_6O_{7.5}(BDC)_{4.5}$	49.20	1.5/6
UiO-66-$(OH)_2$-def	$[Zr_6O_4(OH)_{8.6}(H_2O)_{4.6}(doBDC)_{3.7}]$·solvent	$Zr_6O_{8.3}(doBDC)_{3.7}$	48.00	2.3/6
UiO-66-NH_2-def	$[Zr_6O_4(OH)_{6.2}(H_2O)_{2.2}(BDC\text{-}NH_2)_{4.9}]$·solvent	$Zr_6O_{7.1}(BDC\text{-}NH_2)_{4.9}$	49.50	1.1/6

[a] Experimental data normalized to 100% at 280 °C. [b] A complete release and dehydration and dihydroxylation of the inorganic clusters has been assumed at 280 °C.[41]

Chromium adsorption capacity

After the initial characterization of UiO-66-R samples, the combined effect of the presence of: i) linker defect positions and ii) -NH_2 and -$(OH)_2$ electron-donor groups on the adsorption capacity over Cr^{VI} and Cr^{III} was investigated. It is worth noting that Cr^{VI} is stable as chromate anions in aqueous solutions, whereas Cr^{III} is usually found as oxo-aquo species at acidic conditions. Indeed, for sake of comparison all the experiments developed in this work were performed at pH 3.5. From the adsorbate—adsorbent electrostatic interaction point of view, it is foreseen that the Cr^{III} and Cr^{VI} species behave in different way, since they will be immobilized at different points of the adsorbent chemical structure.

Adsorption isotherms for UiO-66-R (R=-H, -NH_2, -$(OH)_2$, -H-def, -NH_2-def, -$(OH)_2$-def) compounds were obtained from batch experiments of chromium solutions with concentrations ranging from 1 to 100 ppm, as shown in Figure 2. The isotherm curves were fitted by nonlinear Langmuir[63] and Freundlich[5,63,64] models, described in the supplementary information. The experimental data, as well as the modelled adsorption isotherms, are shown in Figure 2. The final adsorption capacity, the adsorption affinity and the correlation parameters obtained from the experimental fittings are summarized in Table 2. The correlation coefficient values (*R* factor) of Freundlich are slightly better than these for Langmuir fitting, pointing that a monolayer homogeneous chromium adsorption process occurs at UiO-66-R materials, as it has been described in previous research.[65]

A marked increase on the capacities for chromate adsorption is observed at the isotherms curve saturation region in defective samples in comparison with nondefective ones. This experimental evidence confirms the importance of linker defective positions at under-coordinated zirconium clusters as adsorption docking points for chromate anions. Moreover, linker functionalization with hydroxy or amine groups further boost the chromate adsorption capacity of UiO-66-R sorbents, an experimental result that points the important role of hydroxy and amine groups in the chromate adsorption.

Therefore, in terms of Cr^{VI} adsorption capacity, the combination of linker defective network with the presence of electron donor hydroxy or amine groups is the best combination to reach the highest possible saturation capacity (i.e., ~40 mg g^{-1}, Figure 2 A–C). It is worth mentioning that, despite the fact that hydroxy and amine functionalized compounds show similar maximum adsorption capacity, the K_L and *n* parameters values obtained from the Langmuir and Freundlich fittings suggest that their chemical affinity towards Cr^{VI} is different.[66–69]

As expected, the opposite trend is observed at Cr^{III} adsorption experiments, as in this case, the higher the concentration of -OH or -NH_2 groups, the higher the Cr^{III} adsorption capacity of the materials, being the linker-defect generation detrimen-

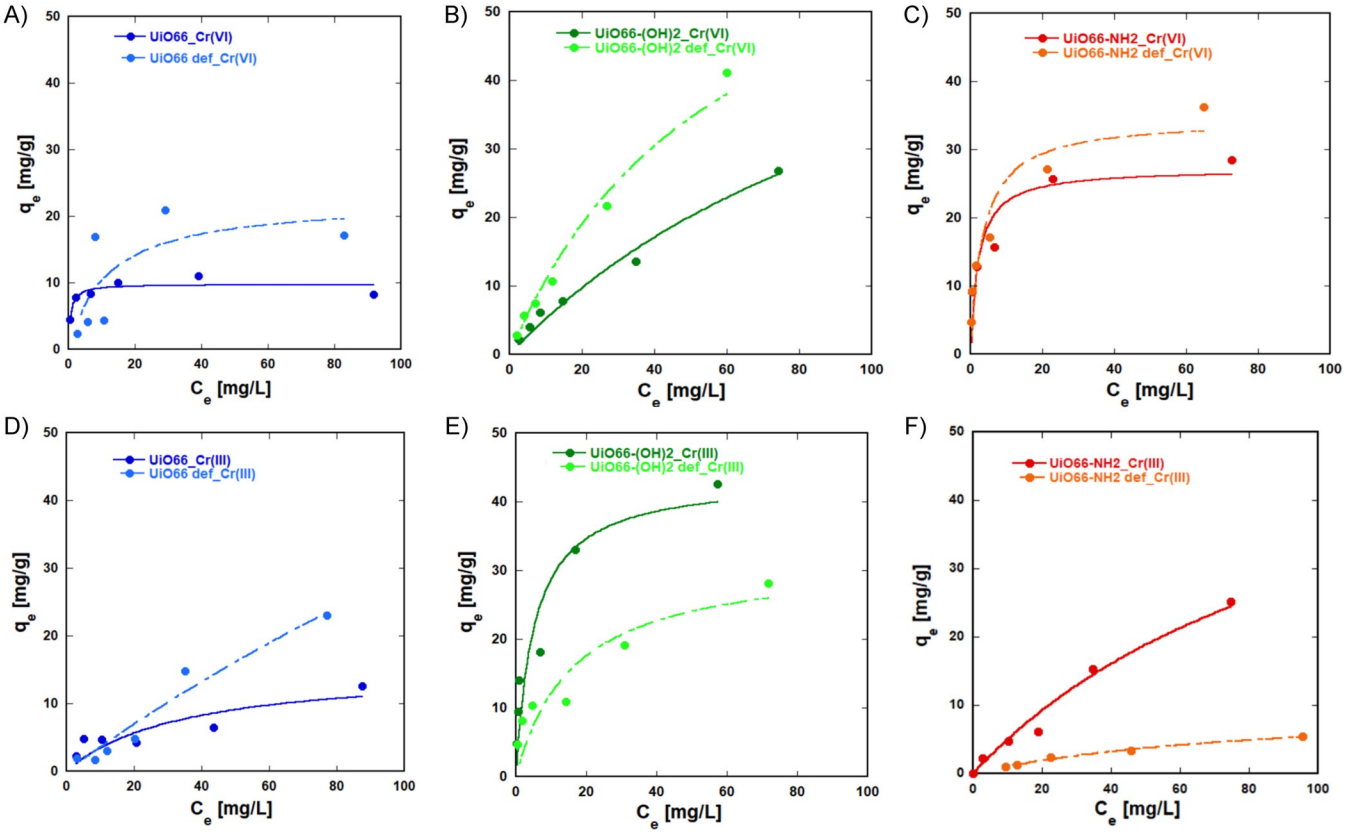

Figure 2. Adsorption isotherms for A–C) Cr^{VI} and D–F) Cr^{III} for UiO-66, and UiO-66-def (A and D), UiO-66-$(OH)_2$ and UiO-66-$(OH)_2$-def (B and E), UiO-66-NH_2 and UiO-66-NH_2-def (C and F). Points: experimental data, line: Langmuir fitting; adsorbent concentration 1 mg mL^{-1}, volume of solution: 10 mL, T=21 °C, pH 4, equilibrium time: 24 h.

Table 2. Parameters obtained for the fitting of the Cr^{VI} and Cr^{III} adsorption isotherms of Figure 2 by nonlinear Langmuir and Freundlich models.

	Langmuir			Freundlich		
	q_m [mg g^{-1}]	K_L [L mg^{-1}]	R^2	K_F [mg^{1-n} L^n g^{-1}]	n	R^2
Hexavalent chromium						
UiO-66	8.8 ± 0.6	1.65 ± 0.72	0.8991	6.6 ± 1.1	10.2 ± 5.5	0.7206
UiO-66-def.	22.4 ± 8.2	0.09 ± 0.08[a]	0.7534	4.3 ± 3.2	2.8 ± 1.7[a]	0.6828
UiO-66-$(OH)_2$	70.8 ± 22.8	0.008 ± 0.004	0.9905	1.02 ± 0.17	1.32 ± 0.07	0.9964
UiO-66-$(OH)_2$-def.	75.5 ± 15.7	0.017 ± 0.006	0.9913	1.58 ± 0.11	1.26 ± 0.03	0.9994
UiO-66-NH_2	27.2 ± 2.9	0.46 ± 0.22	0.9399	10.4 ± 1.1	4.05 ± 0.49	0.9803
UiO-66-NH_2-def.	34.4 ± 4.2	0.29 ± 0.14	0.9442	10.7 ± 0.5	3.39 ± 0.17	0.9968
Trivalent chromium						
UiO-66	15.4 ± 5.9	0.03 ± 0.02[a]	0.8322	1.32 ± 0.61	2.08 ± 0.51	0.9153
UiO-66-def.	_[a]	_[a]	_[a]	0.38 ± 0.24	1.05 ± 0.17	0.9739
UiO-66-$(OH)_2$	43.5 ± 7.4	0.19 ± 0.13	0.9301	11.6 ± 1.6	3.07 ± 0.38	0.9813
UiO-66-$(OH)_2$-def.	31.8 ± 7.9	0.06 ± 0.04	0.8952	5.11 ± 1.04	2.57 ± 0.37	0.9743
UiO-66-NH_2	61 ± 20	0.009 ± 0.004	0.9899	0.69 ± 0.24	1.19 ± 0.12	0.9915
UiO-66-NH_2-def.	10.3 ± 1.2	0.011 ± 0.002	0.9963	0.25 ± 0.04	1.48 ± 0.09	0.9960

[a] The accuracy of the fitting is compromised by the accuracy of the experimental data, especially in these samples with small adsorption capacity values at low concentrations.

tal. In addition, UiO-66-$(OH)_2$ and UiO-66-$(OH)_2$-def compounds are more effective than amine functionalized analogues to sorb Cr^{III} species.

Considering the results as a whole, it can be concluded that the combination of linker defect positions and the presence of -NH_2/-OH groups is the best encoding strategy to adsorb Cr^{VI}, whilst in the case of Cr^{III} immobilization; linker defects are detrimental, being the encoding of hydroxy functionalities the best approach to adsorb it efficiently.

The adsorption kinetics of UiO-66-NH_2 and UiO-66-NH_2-def materials over Cr^{III} and Cr^{VI} were also studied. Adsorption kinetic curve were fitted to pseudo-first-order, pseudo-second-order and Bangham models (Figures S5 and S6). The parameters obtained from the fittings have been summarized in the Table S6.

Based on the kinetic profiles shown in the Figure S5 and S6, the adsorption kinetics are faster for Cr^{VI} adsorption in comparison to Cr^{III}. Following the same tendency observed in the adsorption isotherms, the linker-defective material shows higher uptake capacity over anionic Cr^{VI} species, whereas nondefective UiO-66-NH_2 sorbent shows a better uptake of Cr^{III} cations.

The kinetic profiles for both ions are not well fitted to a first order models (Figure S5), a fact that indicates that the adsorption process is not solely governed by the diffusion of the ions into the UiO-66-NH_2 porous crystal structure. Indeed, the kinetic curves are better simulated when pseudo second order and Bangham models are applied. This tendency suggest that the chromium diffusion is coupled to a posterior chemisorption/reduction process into the MOF structure.

The UiO-66-NH_2 sample was also subjected to a Cr^{VI} to Cr^{III} photo-reduction under UVA and visible light illumination. The main goal of the Cr^{VI} photo-reduction experiments is not only to prove the feasibility of UiO-66-NH_2 samples to phototransform chromate species, since this has been previously corroborated by several research teams,[6,70,71] but to latter compare the chromium speciation stabilized within UiO-66-NH_2 material after operation. To this end, the photo-reduction experiments were performed under ultraviolet and visible light irradiation over a 5 ppm chromate solution with a photocatalyst loading of 0.25 g L^{-1}. The photo-reduction curves shown in Figure S7 confirm that all the chromate species have been reduced to Cr^{III} when the material is exposed to UVA radiation, and nearly the 80% of the chromate is transformed to Cr^{III} under visible illumination. Indeed, the kinetic constants of the photo-reduction processes, obtained from the linear fitting of the data (Figure S7), indicate that the rate of the photo-reduction is doubled when the material is exposed to UVA ($k = 0.10$) in comparison to visible light illumination ($k = 0.05$). Post-operation metal content analysis of the solutions confirmed that the Cr^{III} concentration slightly increase during the photo-reduction, which indirectly points that UiO-66-NH_2 is able to immobilise the most of the transformed Cr^{III} species within its structure.

Adsorbents characterization after operation

XRD patterns of UiO-66-R samples after Cr^{III} and Cr^{VI} adsorption confirm their structural stability upon prolonged exposition to high concentrated chromium (100 ppm) solutions (Figure S8). The crystallinity degree, diffraction maxima position and intensity remain unchanged. In addition, no trace of additional phases have been observed by XRD, a fact that discards that the chromium immobilization occurs through its precipitation as chromium oxide, and that further confirms the adsorption process is the main driving mechanism for Cr^{VI} and Cr^{III} retention within the MOF structure. Samples were also studied by FTIR-ATR (Figure S9), but no significant differences or new bands were observed in the spectra, since the adsorption bands related to chromate vibrational modes are very subtle to be detected.

Amino decorated samples were selected to study their morphology and composition by means of transmission electron microscopy (TEM; Figure S10). All the samples present a nearly spherical shape with a particle size ranging from 20 to 100 nm. More importantly, the TEM images do not show an additional growth of chromium oxide shell layers at the surface of the

MOF nanoparticles, a fact that discards the possibility of chromium oxide precipitation.

Despite no evidences of Cr^{III} and Cr^{VI} post-adsorption structural damage were observed by XRD or FTIR analyses, further investigation of the after-operation thermal stability of UiO-66-NH_2 and UiO-66-NH_2-def samples was carried out. Any structural damage related to cluster-linker bridges partial or complete disruption should be reflected in a lower-temperature structural collapse (Figure S11).[9,72,73]

After a first visual inspection of thermo-diffraction data, no relevant displacements of the diffraction maxima are observed during heating; independently on the sample. Nevertheless, meaningful differences were noticed in the temperature dependent $2\theta(^\circ)$ position and intensity variation of (001) reflection (Figure S11). For UiO-66-NH_2-def, a continuous thermal displacement of the (001) maximum to higher $2\theta(^\circ)$ positions, accentuated above 150 °C, is observed. In parallel, after an initial increase up to 100 °C, the intensity of the (001) reflection is stabilized until it decreases significantly above 250 °C. If both the temperature induced (001) maxima displacement and its intensity loss are considered, the starting point and velocity of the structural collapse can be established at 250 °C.[74]

Thermal stability of UiO-66-NH_2-def is not influenced after the Cr^{III} uptake, as both the shift and intensity loss of (001) diffraction maxima follow the same trend as the pristine sample. Conversely, this is not the case for the sample after the hexavalent chromate adsorption, since an evident structural contraction and intensity reduction is observed above 100 °C, further accentuated above 200 °C.

Surprisingly, the nondefective sample UiO-66-NH_2 shows a less stable thermal dependent behaviour, since the structural contraction, related with the position and intensity variation of the (001) maximum started below 150 °C. For Cr^{III} and Cr^{VI} loaded samples, this initial structural degradation temperature is lowered to 100 °C, being the whole process much more accentuated in comparison to the pristine UiO-66-NH_2 compound. This evidence further reinforces the idea that some local structural damage is produced during the chromium adsorption. Indeed, zirconium-based MOFs are known to be very labile materials that are able to post-synthetically adapt their crystal structure through organic linker exchange. This structural adaptation mechanism can be considered also as one of the driving forces for chromate uptake by UiO-66 materials, since the anionic chromate species could also induce the displacement of carboxyl-zirconium bridges within the UiO-66 frameworks.

Chromium speciation after operation

UV/Vis spectroscopy

The colour change of the studied samples after-adsorption is the first visual evidence indicating the degree of chromium adsorption and reductive capacity of the studied materials (Figure 3 A).

UiO-66 and UiO-66-def samples show a colour change from white to yellow (Cr^{VI}) and light grey (Cr^{III}), respectively. The post-adsorption colours of the studied materials match with the yellow and light green colours usually found for Cr^{VI} and Cr^{III} species, respectively.

The colour change is further accentuated for hydroxy or amine decorated samples. After Cr^{VI} adsorption, UiO-66-NH_2 and UiO-66-$(OH)_2$ compounds acquire a dark brown colour that is indicative of electron transfer process between chromium mixed-valence species. It is worth noting that the same compounds after Cr^{III} adsorption show lighter colours than Cr^{VI} loaded materials. In this case, chromium is solely stabilized as Cr^{III} ions, overriding the electron transfer, and hence, blocking

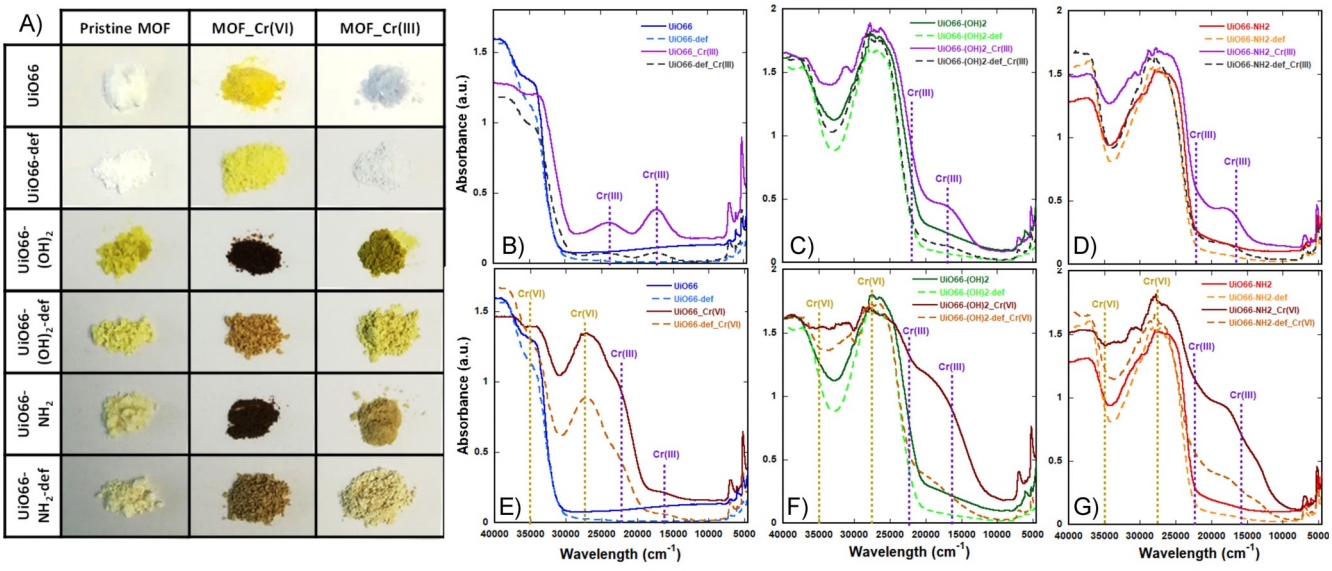

Figure 3. A) Pictures of the samples before and after Cr^{VI} and Cr^{III} adsorption. UV/Vis spectra for UiO-66-R materials before and after B–D) Cr^{III} and E–G) Cr^{VI} adsorption processes. As a guide for the eye, dashed lines have been plotted in the ideal positions for adsorption bands related to Cr^{VI}-O charge transfer processes and octahedral Cr^{III} electronic transitions.

the absorbance increase ascribed to charge transfer processes between chromium ions with difference oxidation states.

Afterwards, chromium speciation within the UiO-66-R was described applying a multi-technique UV/VIS and EPR spectroscopy post-adsorption characterization. UV/Vis spectra of UiO-66 materials show the common fingerprint band located around 35000 cm^{-1} that is attributed to the ligand-to-metal charge transfer (LMCT) (Figure 3B–G). Additional bands located around 27500 cm^{-1} are observed for the functionalized UiO-66-NH_2 and UiO-66-$(OH)_2$ samples, which are associated to the donation of electron density from the hydroxy and amine groups to the π^* orbitals of the benzene ring.

After operation, UV/Vis spectra show additional adsorption bands related to Cr^{VI} and Cr^{III} species. Specifically, samples after Cr^{III} adsorption exhibit (Figure 3B–D) two additional UV/Vis signals associated to the spin-allowed d–d transitions of an octahedral-coordinated $Cr^{3+}d^7$, $^4A_{2g}(F)\rightarrow{}^4T_{1g}(F)$ (UiO-66 $\nu1=$ 23500 cm^{-1}, $\nu1=$UiO-66-def 24000 cm^{-1}) and $^4A_{2g}(F)\rightarrow{}^4T_{2g}(F)$ (UiO-66 $\nu2=$21200 cm^{-1}, UiO-66-def $\nu2=$17200 cm^{-1}, UiO-66-NH_2 $\nu2=$17900 cm^{-1}, UiO-66-NH_2-def $\nu2=$17800 cm^{-1}, UiO-66-$(OH)_2$ $\nu2=$17400 cm^{-1}, UiO-66-$(OH)_2$-def $\nu2=$17000 cm^{-1}). It should be noted that in amine- and hydroxy-functionalized samples, the absorption band associated to the $^4A_{2g}(F)\rightarrow{}^4T_{1g}(F)$ transition is overlapped with the cluster–ligand charge transfer band. Absorbance of UV/Vis signals related to Cr^{III} is higher for -OH- and -NH_2-functionalized nondefective materials; in good agreement with the maximum adsorption capacities observed at the adsorption essays.[23]

The UV/Vis spectra of UiO-66-R compounds after Cr^{VI} adsorption (Figure 3F, G) show the characteristic fingerprints of Cr^{6+}-O^{2-} charge transfer bands for monochromate species at 35000 and 27500 cm^{-1}. For the UiO-66 and UiO-66-def samples, in addition to the above-observed signals, the small absorption peak located around 17000 cm^{-1} confirms the presence of Cr^{III} species within the sorbent. This evidence further points that the Cr^{VI} capture is coupled to its partial reduction to Cr^{III} (Figure 3E, G). The Cr^{VI} to Cr^{III} reductive capacity of the amine- or hydroxy-functionalized UiO-66 frameworks is accentuated (Figure 3E–G), as derived from the absorbance values of the Cr^{III} absorption bands observed in the UV/Vis spectra (UiO-66-NH_2 $\nu2=$17900 cm^{-1}, UiO-66-NH_2-def $\nu2=$17800 cm^{-1}, UiO-66-$(OH)_2$ $\nu1=$23000 cm^{-1} and $\nu2=$16800 cm^{-1}, UiO-66-$(OH)_2$-def $\nu1=$23000 cm^{-1} and $\nu2=$16400 cm^{-1}). As has previously been mentioned, -NH_2 and -OH groups can boost electron transfer processes inducing the chromium reduction. The slight differences observed in the position of the absorption signals can be explained based on slightly different coordination environments of the Cr^{III} ions once stabilized into the UiO-66-R frameworks.

Besides the confirmation of the presence of Cr^{III}, the absorbance increase in the 35000–30000 cm^{-1} UV/Vis region points to the co-existence of Cr^{VI} and Cr^{III} after operation, indicating that the Cr^{VI} to Cr^{III} reduction is not completely effective.

Unsurprisingly, when the adsorption process is coupled to photo-reduction in UiO66-NH_2 photoactive sample, UV/Vis spectrum of UiO-66-NH_2 after operation shows even a higher absorbance of the UV/Vis signals related to the Cr^{III} species. This fact initially suggests that the chromate anions can be further stabilized as Cr^{III} species upon illumination (Figure S13).

Electron paramagnetic resonance spectroscopy

Coupled adsorption-reduction mechanisms in UiO-66-R materials were studied by means of electron paramagnetic resonance (EPR) spectroscopy (Figure 4). Both samples after the Cr^{VI} and Cr^{III} adsorption, as well and UiO66-NH_2 sample after the photo-reduction experiment were studied by EPR. Generally speaking, three different signals associated to Cr^{III} and Cr^{V} species can be observed by EPR:

γ-signal: This axially symmetric intense and sharp adsorption band located around 3400 G is ascribed to an isolated Cr^{5+}, which usually presents a highly distorted octahedral or pseudo-pyramidal coordination environment. γ-signals exhibit a characteristic sharp g_x and a weak somewhat diffuse g_{II} line. The axial rhombic distortion of Cr^{V} could explain the broader

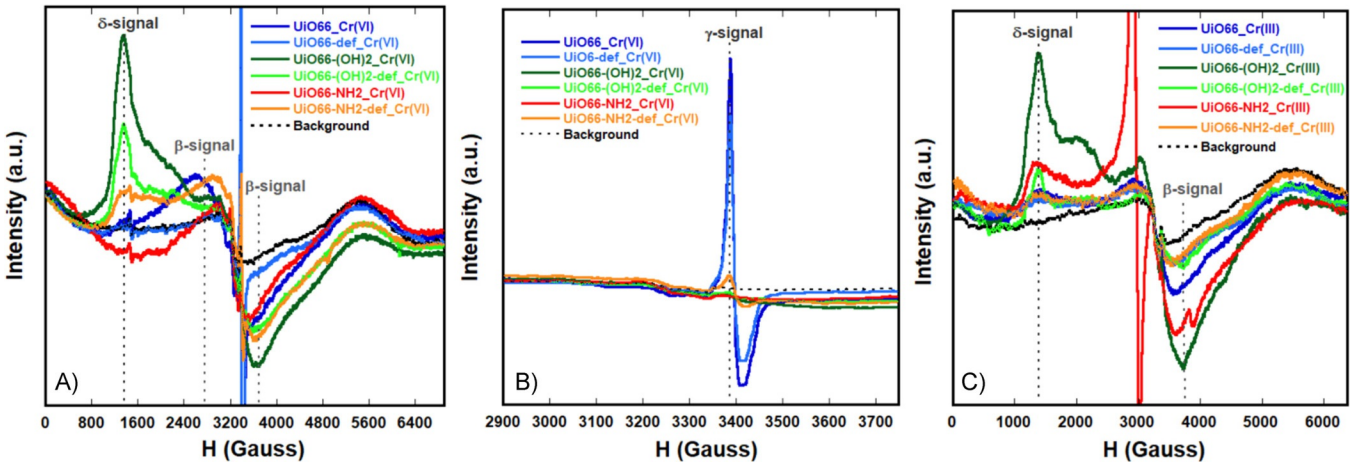

Figure 4. A) EPR spectra of UiO-66-R after Cr^{VI} uptake highlighting the δ and β-signals associated with Cr^{III} species. B) Detail of the 3200–3600 Gauss interval of the EPR spectra showing the γ-signal ascribed to isolated Cr^{V} ions. C) EPR spectra of UiO-66-R after Cr^{III} adsorption.

and less intense signals between 3400 and 3450 G fields (Figure 4 B).

δ-signal: This dispersed adsorption band located about 1300 G is related with Cr^{III} isolated species (Figure 4 A and C).

β-signal: This broad isotropic absorption band is related with the Cr^{III} magnetically coupled systems, which g value strongly depends on the size and shape of the chromium clusters (Figure 4 A and C). The presence of this characteristic EPR fingerprint indicates that the Cr^{III} ions are immobilized within the UiO-66 matrix close enough to stablish magnetic interactions, which in terms of local structure can be explained as the presence of Cr^{III}-*O*-Cr^{III} or Cr^{III}-OH···O-Cr^{III} bridges within the pores of the UiO-66 framework.[31]

Cr^{VI} is silent by EPR, but it is worthy to note that its presence has been previously confirmed by UV/Vis. The EPR spectra of the Cr^{VI} post-adsorption samples are described and depicted in the Figure 4. A comparison between the EPR spectra confirms that the presence of γ, δ and β-signals are associated to the existence of Cr^{III} and Cr^{V} in all the samples, but the intensity ratio between them is highly dependent on the functionalization groups or defect degree of the UiO-66 derivatives.

Given the presence of reduced chromium species for all the samples after chromate adsorption, it can be generally concluded that the capture of Cr^{VI} by UiO-66-R materials is not just an adsorption process, but also involves electron transfer that induces the reduction of chromate anions to Cr^{V} and Cr^{III}. When comparing the absorbance of the EPR signals for the different UiO-66-R samples, a qualitative estimation of the reduction capacity can be estimated. The reductive capacity of UiO-66-R materials is highly dependent of the linker functionalization and/or on the presence of defect points in the crystal structure. UiO-66-NH_2 and UiO-66-$(OH)_2$ compounds exhibit more intense δ and β-signals ascribed to the presence of Cr^{III} species, which indicates that the -NH_2 and -OH electron-donor groups shifts the post-adsorption chromium equilibrium towards reduced species, such as Cr^{V} and Cr^{III}. Contrarily, EPR spectra of non-functionalized UiO-66 materials exhibit only the characteristic γ-signal of transient Cr^{5+} ions, that together with the Cr^{6+} species detected by UV/Vis spectroscopy, drawn a Cr^{6+} and Cr^{5+} speciation mixture stabilized within the sorbent after operation. Therefore, the lack of electron donors at the UiO-66 framework limits the reductive capacity of non-functionalized materials. In addition, Cr^{VI} to Cr^{III} reduction is less effective in defective functionalized UiO-66-$(OH)_2$-def and UiO-66-NH_2-def samples, since the absorbance of β and δ-signals ascribed to Cr^{III} is lower.

The comparison of EPR spectra of UiO-66-NH_2 after Cr^{VI} adsorption and Cr^{VI} to Cr^{III} photo-reduction experiments, confirms that the concentration of Cr^{V} transient species stabilized within the matrix is significantly reduced after illumination, whereas the Cr^{III} ions concentration increases (Figure S14 a). Therefore, upon illumination, photocatalytic activity of UiO-66-NH_2 displaces in more extent the reduction process to Cr^{III} species, but without achieving the complete conversion of Cr^{VI} to Cr^{III}, as Cr^{V} species are still detected (Figure S14 b).

Proposed chromium adsorption-reduction coupled mechanisms

Before tackling the explanation of the possible chromium adsorption-reduction mechanisms in UiO-66-R materials, it is necessary to introduce a brief description of the chromium speciation of the model solutions that have been used to perform the adsorption and reduction processes. pH and concentration dependence of Cr^{VI} and Cr^{III} speciation have been calculated and plotted in the Figures S15 to S17. Since the adsorption and photo-reduction experiments have been carried out at acidic pH values (i.e., 3.5), the speciation in this region of the concentration/pH diagrams will be described. Hexavalent chromate is stabilized as hydrogen chromate $(HCrO_4)^-$ and dichromate $(Cr_2O_7)^{2-}$ species at acidic conditions. The dihydrogen chromate anion is also present, but at much lower concentration than the previously mentioned species (Figure S15).

Trivalent chromium is stabilized mainly as monomeric and trimeric species. The hexa-aquo monomeric cation $(Cr(H_2O)_6)^{3+}$ and its partially hydroxylated forms (i.e., $(Cr(H_2O)_5(OH))^{2+}$ and $(Cr(H_2O)_4(OH)_2)^-$…) are the most abundant species in acidic solutions. However, the presence of trimeric ($((Cr_3(H_2O)_9(OH)_4)^{5+}$) and dimeric species ($((Cr_2(H_2O)_8(OH)_4)^{4+}$) is not negligible, and more probably they could take part also in the adsorption process (Figure S16). The possible chemical structures of the Cr^{III} species have been plotted in the Figure S18.

It is important to note that in this work model Cr^{VI} and Cr^{III} solutions have been used, but in a real aqueous environment, the chromium speciation is highly dependent on the Eh, which variation can shift the equilibrium between Cr^{VI} and Cr^{III} species through reduction and oxidation processes.

Taking all this information into consideration, a simplified model for the adsorption, chemical reduction and photoreduction of Cr^{VI} and Cr^{III} species in UiO-66-R materials have been proposed.

Previous research on adsorption mechanisms of oxyanions by zirconium-based MOFs points towards the importance of uncoordinated positions at the inorganic clusters as active chemisorption docking points. Indeed, the local structure of selenite/selenate anions immobilized within NU-1000 crystal structure, which was obtained from a combined analysis of X-ray absorption and pair distribution function, confirms the direct coordination of selenite/selenate groups to the linker defect ordered positions of the zirconium hexanuclear units.[44,75] Similarly, the local structure of sulfated MOF-808, obtained by single crystal X-ray diffraction, shows the same binding mechanism for sulfate anions.[45]

Nevertheless, the chromate immobilization mechanisms studied in this work goes beyond a single adsorption process, since involve also its posterior reduction to Cr^{III}, together with a last clustering step of the Cr^{III} ions.

The proposed simplified mechanism leading to the chromium adsorption and reduction in UiO-66-R samples has been schematically represented in Figure 5.

Assuming that chromate or dichromate anions establish a coordinate covalent bond with the zirconium clusters after the adsorption stage (Figure 5 A), their posterior transformation to

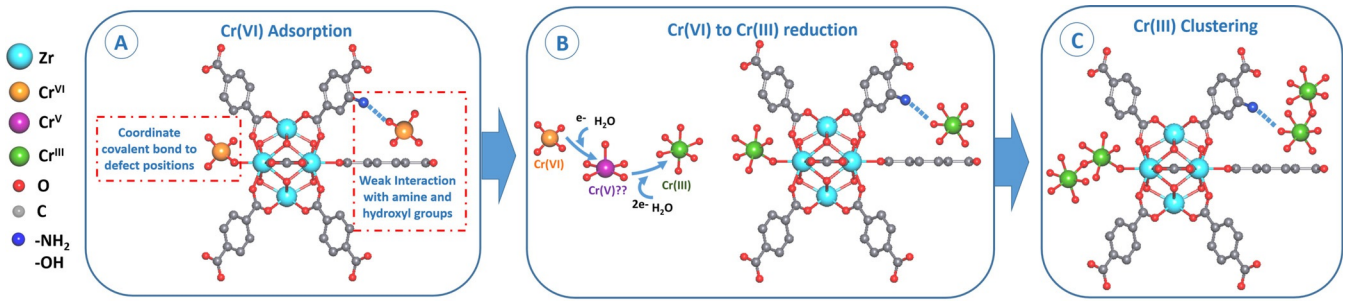

Figure 5. Proposed Cr^{VI} adsorption and Cr^{VI}-to-Cr^{III} reduction mechanisms in UiO66-R type frameworks. A) $Cr^{VI} \rightarrow Cr^{V} \rightarrow Cr^{III}$ reduction at the inorganic clusters, B) $Cr^{VI} \rightarrow Cr^{V} \rightarrow Cr^{III}$ reduction at the linkers, and C) $Cr^{VI} \rightarrow Cr^{V} \rightarrow Cr^{III}$ reduction at the inorganic clusters and the linkers.

Cr^{V} and Cr^{III} is foreseen to occur through the modification of their coordination sphere (Figure 5 B).[32,76] Since at acidic solutions a mixture of hydrogen chromate and dichromate species can be found in similar concentrations, the first chemisorption step can occur indifferently for both species. The possible structural model after the hydrogen chromate chemisorption has been illustrated in the Figure 5 A.

Starting from the less complex scenario, in UiO-66 nonfunctionalized samples, the chromate immobilization it is foreseen to occur through its coordinate covalent bonding to the zirconium clusters (Figure 5 A). Afterwards, the Cr^{VI} partial reduction to Cr^{V} transient species can be achieved by an electron transfer process to the adsorbed species, together with the incorporation of hydroxy or water molecules to the coordination sphere of chromium pentavalent ions (Figure 5 B).

Further Cr^{V} to Cr^{III} reduction would require from a transformation of the five-coordination environment usually shown by Cr^{V} ions, to a six-coordinated octahedral one usually shown by Cr^{III} oxo-aquo species (Figure 5 B). In the last step, the clustering of Cr^{III} species can be achieved by a posterior grafting and reduction of chromate species into the first anchored Cr^{III} ions, as it can be observed in the schematic representation in Figure 5 C. Assuming that a dichromate anion is adsorbed at the first stage of the process, its reduction to Cr^{III} would lead also to clustered Cr^{III} ions stabilized within the UiO-66 framework.

The local structure proposed in the Figure 5 C is in agreement with previously reported ones for single cobalt[77] and tetranuclear cluster catalyst[78] immobilized at Zr-based NU-1000 structures by atomic layer deposition.

As stated before, the presence of hydroxy or amine electron-donor groups at the organic linkers of UiO-66 materials enhance the chromium adsorption and vary the final Cr^{III} clustering degree. Indeed, it is reasonable to assume that chromate and dichromate adsorption takes place through hydrogen bonding or electrostatic interactions at these positions of the UiO-66-R structures. Afterwards, chromium reduction would evolve similarly than for the chromate anions chemisorbed at the inorganic clusters positions (Figure 5 B, C).

Direct adsorption of Cr^{III} ions is foreseen to occur through the establishment of weak host-guess electrostatic and/or hydrogen bonding interactions. The results drawn by EPR spectroscopy confirm the presence of isolated and clustered Cr^{III} species after the adsorption experiments for all the samples. Nevertheless, the ratio between the isolated and clustered Cr^{III} ions varies depending on the defect degree or functionalization motifs of the UiO-66-R compounds (Figure S19). Considering the Cr^{III} speciation equilibrium in solution, it is not surprising that UiO-66-R materials can directly adsorb not only monomeric hexa-aquo cationic species ($((Cr(H_2O)_6)^{3+}$) from solution, but also the dimeric ($(Cr_2(H_2O)_8(OH)_4)^{4+}$) and trimeric ($((Cr_3(H_2O)_9(OH)_4)^{5+}$) clustered species.

Conclusions

UiO-66-R derivative compounds have been synthesized varying the linker functionalization types and linker defect degree in their structures. The influence of these modifications on the Cr^{VI} and Cr^{III} adsorption and reductive capacity of the materials have been confirmed. Considering the maximum adsorption capacity of the studied MOFs, the combined incorporation of -OH and -NH_2 electron-donor groups and generation of linker defective positions is the most favourable MOF chemical encoding approach to enhance the capture of chromate anions. The presence of amino and hydroxy groups is also key to enhance the Cr^{III} adsorption capacity of UiO-66-R materials, but in contrast to Cr^{VI} adsorption, the induction of linker defects within the UiO-66-R frameworks is detrimental in terms of Cr^{III} retention.

The post-adsorption characterization of chromium speciation in UiO-66-R samples reveals that a mixture of Cr^{VI}, Cr^{V} and Cr^{III} isolated and clustered species are stabilized within the sorbents. The presence of hydroxy and amino electron-donor groups promotes the stabilization of chromium as trivalent ions, whilst concentration of Cr^{VI} and Cr^{V} highly reactive species is higher at non-functionalized UiO-66 and UiO-66-def samples.

The reduction of Cr^{VI} to Cr^{III} is further enhanced after the photo-reduction experiments performed with UiO-66-NH_2 photo-active material, but still without achieving the full Cr^{VI} to Cr^{III} transformation.

Our findings point toward a first step chromate chemisorption i) at the clusters under-coordinated position ii) and/or through electrostatic interactions at the hydroxy/amine groups located at the organic linkers. Afterwards, the Cr^{VI} to Cr^{V} and Cr^{III} reduction is foreseen to occur through electron transfer and reorganization of their coordination environment. Further

adsorption and reduction steps can give rise to the clustering of the Cr^{III} species within the pore space of the UiO-66-R frameworks.

Despite the reductive capacity of -NH_2 and -OH electron-donor groups, the full reduction to Cr^{III} is not achieved in any of the studied cases. Cr^{VI} to Cr^{III} photo-reduction further displaces the equilibrium towards reduced Cr^{III}, but after operation, UiO-66-NH_2 photoactive materials still show highly reactive Cr^{VI} and Cr^{V} ions.

The multivariate encoding of -OH_2, -NH_2 and defective position within the same UiO-66-R material can be one of the possible approaches to obtain a completely shifted equilibrium towards Cr^{III} during adsorption of photo-reduction. In addition to the increase of the Cr^{VI} adsorptive capacity induced by the combination of hydroxy groups and under-coordinated positions, the presence of -NH_2 groups at the organic linkers can provide to these materials of an intrinsic photo-activity, which can further enhance the reductive function of the hydroxy motifs.

Finally, it is worth mentioning that the potentials of this research goes beyond the fundamental understanding of chromium speciation within UiO-66-R type MOFs, since the combined UV/Vis and EPR methodology applied in this research can be extended to other Cr^{VI} MOF sorbents and photo-catalysts in order to quantitatively assess their Cr^{VI} to Cr^{III} reductive capacity.

Experimental Section

MOF synthesis: defect engineering

MOFs were prepared through a slightly modified solvothermal synthesis procedure based on the previously reported one by Audu et al.[46] After that, the samples were washed with methanol under stirring during 24 h, centrifuged at 7000 rpm and dispersed again in fresh methanol. The solvent exchange process was repeated three times in order to remove the unreacted ligand and exchange the residual DMF present at the pores. A schematic diagram of the synthesis process is given in Figure S20. Subsequently, the samples were activated at 80 °C during 24 h before each measurement.

The hydroxy (UiO-66-$(OH)_2$) and amine (UiO-66-NH_2) derivatives were synthesised in the same conditions that UiO-66, but using the same molar amounts of 2,5-dihydroxyterephthalic acid (doBDC) and 2-aminoterephthalic acid instead of terephthalic acid (Figure S21). On the other hand, the three analogue linker defective samples (UiO-66-def, UiO-66-$(OH)_2$-def and UiO-66-NH_2-def were synthesised by adding concentrated HCl to the synthesis medium. The parameters used on the different reactions carried out are presented in Table S1.

Adsorption and photo-reduction experiments

In order to carry out the chromium adsorption experiments, stock solutions of 200 ppm of potassium dichromate ($K_2Cr_2O_7$) and of chromium chloride ($CrCl_3$) were prepared. Then, solutions with different concentrations were obtained by diluting the stock solutions with deionized water. pH of the chromium solutions prepared for the adsorption experiments was kept below 3.5 to prevent the precipitation of chromium oxide. The adsorbent dosage was fixed to 1 g L^{-1} for all the adsorption experiments.

Photo-reduction experiments with the UiO-66-NH_2 sample were conducted at room temperature, using a photo-catalyst dosage of 0.25 g L^{-1} and 200 mL 5 ppm Cr^{VI} solution. Photo-reduction experiments were conducted after an hour of adsorption in dark (once reached the adsorption equilibrium). Experiments were performed during 4 h under UVA light. Chromium solutions during the photo-reduction experiments were analysed by the diphenyl carbazide protocol.[2]

Sample characterization

Experimental methodology for the full characterization of the samples before and after chromium adsorption experiments is described in the Supporting Information.

Acknowledgements

The authors thank financial support from the Spanish Ministry of Economy and Competitiveness (MINECO) through projects MAT2016-76739-R (AEI/FEDER, EU) and MAT2016-76039-C4-3-R (AEI/FEDER, UE) (including FEDER financial support) and from the Basque Government Industry and Education Departments under the ELKARTEK (LION, ACTIMAT), HAZITEK (SIMAN) and PIBA (PIBA-2018-06) programs, respectively. The European Commission Research & Innovation H2020-MSCA-RISE-2017 (ref.: 778412) INDESMOF project is also acknowledged as well as the technicians of SGIker (UPV/EHU).

Conflict of interest

The authors declare no conflict of interest.

Keywords: adsorption · chromium · electron paramagnetic spectroscopy · metal–organic frameworks · water remediation

[1] A. Azimi, A. Azari, M. Rezakazemi, M. Ansarpour, *ChemBioEng Rev.* **2017**, *4*, 37 – 59.
[2] H. Sereshti, M. Vasheghani Farahani, M. Baghdadi, *Talanta* **2016**, *146*, 662 – 669.
[3] E. Saadaoui, N. Ghazel, C. Ben Romdhane, N. Massoudi, *Int. J. Environ. Stud.* **2017**, *74*, 558 – 567.
[4] H. Ali, E. Khan, I. Ilahi, *J. Chem.* **2019**, *2019*, 6730305.
[5] M. Czikkely, E. Neubauer, I. Fekete, P. Ymeri, C. Fogarassy, *Water* **2018**, *10*, 1377.
[6] X. D. Du, X. H. Yi, P. Wang, W. Zheng, J. Deng, C. C. Wang, *Chem. Eng. J.* **2019**, *356*, 393 – 399.
[7] X. Li, H. Xu, F. Kong, R. Wang, *Angew. Chem. Int. Ed.* **2013**, *52*, 13769 – 13773; *Angew. Chem.* **2013**, *125*, 14014 – 14018.
[8] B. Ding, J. Z. Huo, Y. Y. Liu, X. Wang, X. Su, X. X. Wu, Z. Z. Zhu, J. Xia, *RSC Adv.* **2015**, *5*, 83415 – 83426.
[9] H. R. Fu, Z. X. Xu, J. Zhang, *Chem. Mater.* **2015**, *27*, 205 – 210.
[10] B. Ding, C. Guo, X. Liu, Y. Cheng, X. Wu, M. Su, *RSC Adv.* **2016**, *6*, 33888 – 33900.
[11] A. V. Desai, B. Manna, A. Karmakar, A. Sahu, S. K. Ghosh, *Angew. Chem. Int. Ed.* **2016**, *55*, 7811 – 7815; *Angew. Chem.* **2016**, *128*, 7942 – 7946.
[12] A. Maleki, B. Hayati, M. Naghizadeh, S. W. Joo, *J. Ind. Eng. Chem.* **2015**, *28*, 211 – 216.
[13] N. Unceta, F. Séby, J. Malherbe, O. F. X. Donard, *Anal. Bioanal. Chem.* **2010**, *397*, 1097 – 1111.
[14] M. B. Arain, I. Ali, E. Yilmaz, M. Soylak, *TrAC Trends Anal. Chem.* **2018**, *103*, 44 – 55.
[15] R. Rakhunde, L. Deshpande, H. D. Juneja, *Crit. Rev. Environ. Sci. Technol.* **2012**, *42*, 776 – 810.

[16] R. Fernández De Luis, A. Martínez-Amesti, E. S. Larrea, L. Lezama, A. T. Aguayo, M. I. Arriortua, *J. Mater. Chem. A* **2015**, *3*, 19996 – 20012.
[17] Z. Fang, M. Zhao, H. Zhen, L. Chen, P. Shi, Z. Huang, *PLoS One* **2014**, *9*, e103194.
[18] A. Chiu, X. L. Shi, W. K. P. Lee, R. Hill, T. P. Wakeman, A. Katz, B. Xu, N. S. Dalal, J. D. Robertson, C. Chen, N. Chiu, L. Donehower, *J. Environ. Sci. Health Part C* **2010**, *28*, 188 – 230.
[19] Y. Wang, H. Su, Y. Gu, X. Song, J. Zhao, *Onco. Targets. Ther.* **2017**, *10*, 4065 – 4079.
[20] R. N. Bose, B. S. Fonkeng, *Chem. Commun.* **1996**, 2211 – 2212.
[21] A. Helal, M. N. Shaikh, A. Aziz, *J. Photochem. Photobiol. A Chem.* **2020**, *389*, 112238.
[22] Z. J. Lin, H. Q. Zheng, H. Y. Zheng, L. P. Lin, Q. Xin, R. Cao, *Inorg. Chem.* **2017**, *56*, 14178 – 14188.
[23] A. Węgrzyniak, A. Rokicińska, E. Hédrzak, B. Michorczyk, K. Zeńczak-Tomera, P. Kuśtrowski, P. Michorczyk, *Catal. Sci. Technol.* **2017**, *7*, 6059 – 6068.
[24] X. Zhang, B. Shen, S. Zhu, H. Xu, L. Tian, *J. Hazard. Mater.* **2016**, *320*, 556 – 563.
[25] M. Jaber, F. Ribot, L. Binet, V. Briois, S. Cassaignon, K. J. Rao, J. Livage, N. Steunou, *J. Phys. Chem. C* **2012**, *116*, 25126 – 25136.
[26] L. Valenzano, B. Civalleri, S. Chavan, S. Bordiga, M. H. Nilsen, S. Jakobsen, K. P. Lillerud, C. Lamberti, *Chem. Mater.* **2011**, *23*, 1700 – 1718.
[27] L. Chen, Z. Bai, L. Zhu, L. Zhang, Y. Cai, Y. Li, W. Liu, Y. Wang, L. Chen, J. Diwu, J. Wang, Z. Chai, S. Wang, *ACS Appl. Mater. Interfaces* **2017**, *9*, 32446 – 32451.
[28] S. Chavan, J. G. Vitillo, M. J. Uddin, F. Bonino, C. Lamberti, E. Groppo, K. P. Lillerud, S. Bordiga, *Chem. Mater.* **2010**, *22*, 4602 – 4611.
[29] B. V. Padlyak, J. Kornatowski, G. Zadrozna, M. Rozwadowski, A. Gutsze, *J. Phys. Chem. A* **2000**, *104*, 11837 – 11843.
[30] P. Michorczyk, P. Pietrzyk, J. Ogonowski, *Microporous Mesoporous Mater.* **2012**, *161*, 56 – 66.
[31] B. M. Weckhuysen, R. A. Schoonheydt, F. E. Mabbs, D. Collison, *J. Chem. Soc. Faraday Trans.* **1996**, *92*, 2431 – 2436.
[32] B. M. Weckhuysen, R. Ramachandra Rao, J. Pelgrims, R. A. Schoonheydt, P. Bodart, G. Debras, O. Collart, P. Van Der Voort, E. F. Vansant, *Chem. Eur. J.* **2000**, *6*, 2960 – 2970.
[33] A. Levina, A. M. Bailey, G. Champion, P. A. Lay, *J. Am. Chem. Soc.* **2000**, *122*, 6208 – 6216.
[34] V. Daier, S. Signorella, M. Rizzotto, M. I. Frascaroli, C. Palopoli, C. Brondino, J. M. Salas-Peregrin, L. F. Sala, *Can. J. Chem.* **1999**, *77*, 57 – 64.
[35] Z. Hu, I. Castano, S. Wang, Y. Wang, Y. Peng, Y. Qian, C. Chi, X. Wang, D. Zhao, *Cryst. Growth Des.* **2016**, *16*, 2295 – 2301.
[36] T. Stassin, H. Reinsch, B. Van de Voorde, S. Wuttke, D. D. Medina, N. Stock, T. Bein, R. Ameloot, D. De Vos, *ChemSusChem* **2017**, *10*, 643 – 650.
[37] S. Øien, D. Wragg, H. Reinsch, S. Svelle, S. Bordiga, C. Lamberti, K. P. Lillerud, *Cryst. Growth Des.* **2014**, *14*, 5370 – 5372.
[38] K. A. Lin, S. Chen, A. P. Jochems, *Mater. Chem. Phys.* **2015**, *160*, 168 – 176.
[39] C. Serre, T. Devic, *The Chemistry of Metal – Organic Frameworks: Synthesis, Characterization, and Applications* (Ed.: S. Kaskel), Wiley-VCH, Weinheim, Vol. 1, **2016**, pp. 171 – 202.
[40] M. M. Modena, B. Rühle, T. P. Burg, S. Wuttke, *Adv. Mater.* **2019**, *31*, 1970226.
[41] G. C. Shearer, S. Chavan, J. Ethiraj, J. G. Vitillo, S. Svelle, U. Olsbye, C. Lamberti, S. Bordiga, K. P. Lillerud, *Chem. Mater.* **2014**, *26*, 4068 – 4071.
[42] G. C. Shearer, S. Chavan, S. Bordiga, S. Svelle, U. Olsbye, K. P. Lillerud, *Chem. Mater.* **2016**, *28*, 3749 – 3761.
[43] A. R. Muguruza, R. F. de Luis, N. Iglesias, B. Bazán, M. K. Urtiaga, E. S. Larrea, A. Fidalgo-Marijuan, G. Barandika, *J. Inorg. Biochem.* **2020**, *205*, 110977.
[44] A. J. Howarth, M. J. Katz, T. C. Wang, A. E. Platero-Prats, K. W. Chapman, J. T. Hupp, O. K. Farha, *J. Am. Chem. Soc.* **2015**, *137*, 7488 – 7494.
[45] J. Jiang, F. Gándara, Y. B. Zhang, K. Na, O. M. Yaghi, W. G. Klemperer, *J. Am. Chem. Soc.* **2014**, *136*, 12844 – 12847.
[46] C. O. Audu, H. G. T. Nguyen, C.-Y. Chang, M. J. Katz, L. Mao, O. K. Farha, J. T. Hupp, S. T. Nguyen, *Chem. Sci.* **2016**, *7*, 6492 – 6498.
[47] C. Wang, X. Liu, J. P. Chen, K. Li, *Sci. Rep.* **2015**, *5*, 16613.
[48] J. Luo, F. Xu, J. Hu, P. Lin, J. Tu, X. Wu, X. Hou, *Microchem. J.* **2017**, *133*, 441 – 447.
[49] A. Nasrollahpour, S. E. Moradi, *Microporous Mesoporous Mater.* **2017**, *243*, 47 – 55.
[50] Z. Wang, J. Yang, Y. Li, Q. Zhuang, J. Gu, *Chem. Eur. J.* **2017**, *23*, 15415 – 15423.
[51] S. Wang, T. Kitao, N. Guillou, M. Wahiduzzaman, C. Martineau-Corcos, F. Nouar, A. Tissot, L. Binet, N. Ramsahye, S. Devautour-Vinot, S. Kitagawa, S. Seki, Y. Tsutsui, V. Briois, N. Steunou, G. Maurin, T. Uemura, C. Serre, *Nat. Commun.* **2018**, *9*, 1660.
[52] S. Zhao, G. Wang, D. Poelman, *Molecules* **2018**, *23*, 2947.
[53] J. Bedia, V. Muelas-Ramos, M. Peñas-Garzón, A. Gómez-Avilés, J. J. Rodríguez, C. Belver, *Catalysts* **2019**, *9*, 52.
[54] H. Zhao, Q. Xia, H. Xing, D. Chen, H. Wang, *ACS Sustainable Chem. Eng.* **2017**, *5*, 4449 – 4456.
[55] J. Matos, M. Rosales, A. García, C. Nieto-Delgado, J. R. Rangel-Mendez, *Green Chem.* **2011**, *13*, 3431 – 3439.
[56] M. Rosales, T. Zoltan, C. Yadarola, E. Mosquera, F. Gracia, A. García, *J. Mol. Liq.* **2019**, *281*, 59 – 69.
[57] N. Yin, K. Wang, L. Wang, Z. Li, *Chem. Eng. J.* **2016**, *306*, 619 – 628.
[58] S. Wu, Y. Ge, Y. Wang, X. Chen, F. Li, H. Xuan, X. Li, *Environ. Technol.* **2018**, *39*, 1937 – 1948.
[59] K. Wang, J. Gu, N. Yin, *Ind. Eng. Chem. Res.* **2017**, *56*, 1880 – 1887.
[60] H. Fei, C. S. Han, J. C. Robins, S. R. J. Oliver, *Chem. Mater.* **2013**, *25*, 647 – 652.
[61] J. Hajek, C. Caratelli, R. Demuynck, K. De Wispelaere, L. Vanduyfhuys, M. Waroquier, V. Van Speybroeck, *Chem. Sci.* **2018**, *9*, 2723 – 2732.
[62] G. C. Shearer, S. Forselv, S. Chavan, S. Bordiga, K. Mathisen, M. Bjørgen, S. Svelle, K. P. Lillerud, *Top. Catal.* **2013**, *56*, 770 – 782.
[63] S. J. Allen, G. Mckay, J. F. Porter, *J. Colloid Interface Sci.* **2004**, *280*, 322 – 333.
[64] S. Chowdhury, R. Mishra, P. Saha, P. Kushwaha, *Desalination* **2011**, *265*, 159 – 168.
[65] J. Li, X. Wang, G. Zhao, C. Chen, Z. Chai, A. Alsaedi, T. Hayat, X. Wang, *Chem. Soc. Rev.* **2018**, *47*, 2322 – 2356.
[66] J. A. González, M. E. Villanueva, L. L. Piehl, G. J. Copello, *Chem. Eng. J.* **2015**, *280*, 41 – 48.
[67] D. I. Torres, J. M. Lazaro-Martínez, G. J. Copello, V. C. dall Orto, *J. Environ. Chem. Eng.* **2019**, *8*, 103416.
[68] J. A. González, M. E. Villanueva, M. L. Peralta Ramos, C. J. Pérez, L. L. Piehl, G. J. Copello, *RSC Adv.* **2015**, *5*, 63813 – 63820.
[69] M. L. Peralta Ramos, J. A. González, S. G. Albornoz, C. J. Pérez, M. E. Villanueva, S. A. Giorgieri, G. J. Copello, *Chem. Eng. J.* **2016**, *285*, 581 – 587.
[70] R. Bibi, Q. Shen, L. Wei, D. Hao, N. Li, J. Zhou, *RSC Adv.* **2018**, *8*, 2048 – 2058.
[71] Y. Feng, Q. Chen, M. Cao, N. Ling, J. Yao, *ACS Appl. Nano Mater.* **2019**, *2*, 5973 – 5980.
[72] L. Huang, M. He, B. Chen, B. Hu, *J. Mater. Chem. A* **2016**, *4*, 5159 – 5166.
[73] W. Morris, S. Wang, D. Cho, E. Auyeung, P. Li, O. K. Farha, C. A. Mirkin, *ACS Appl. Mater. Interfaces* **2017**, *9*, 33413 – 33418.
[74] G. Mouchaham, S. Wang, C. Serre, in *Metal – Organic Frameworks: Applications in Separations and Catalysis* (Eds.: H. García, S. Navalón), Wiley-VCH, Weinheim, **2018**, pp. 1 – 28.
[75] H. Ouyang, N. Chen, G. Chang, X. Zhao, Y. Sun, S. Chen, H. Zhang, D. Yang, *Angew. Chem. Int. Ed.* **2018**, *57*, 13197 – 13201; *Angew. Chem.* **2018**, *130*, 13381 – 13385.
[76] D. Rai, B. M. Sass, D. A. Moore, *Inorg. Chem.* **1987**, *26*, 345 – 349.
[77] Z. Li, A. W. Peters, V. Bernales, M. A. Ortuño, N. M. Schweitzer, M. R. Destefano, L. C. Gallington, A. E. Platero-Prats, K. W. Chapman, C. J. Cramer, L. Gagliardi, J. T. Hupp, O. K. Farha, *ACS Cent. Sci.* **2017**, *3*, 31 – 38.
[78] Z. Li, N. M. Schweitzer, A. B. League, V. Bernales, A. W. Peters, A. B. Getsoian, T. C. Wang, J. T. Miller, A. Vjunov, J. L. Fulton, J. A. Lercher, C. J. Cramer, L. Gagliardi, J. T. Hupp, O. K. Farha, *J. Am. Chem. Soc.* **2016**, *138*, 1977 – 1982.

Manuscript received: March 24, 2020
Accepted manuscript online: June 17, 2020
Version of record online: October 4, 2020